communications engineering

A Nature Portfolio journal

Article

https://doi.org/10.1038/s44172-025-00425-2

Flexible screen-printed *SiC*-based humidity sensors

Arjun Wadhwa [1], Alexandre Perrotton [1], Mohamad Hassan Taherian [2], Abbas Zirakjou [1], Jaime Benavides-Guerrero [1], Mathieu Gratuze [1], Fabrice Vaussenat [1], Martin Bolduc [2] & Sylvain G. Cloutier [1] ✉

Humidity sensors are essential components in modern technology, spanning applications from residential appliances to the Internet of Things (IoT). However, conventional commercial sensors are typically rigid, constrained by narrow relative humidity (%RH) operating ranges, and require complex fabrication processes. In this study, we present a highly sensitive cubic silicon carbide (3C–SiC) nanoparticle-based relative humidity sensor, fabricated via serigraphic printing on to 5 mil thick flexible polyimide (Kapton®) substrate. Devices are tested across a broad humidity range of 10–90%RH at ambient temperature and their performance is evaluated in a controlled humidity chamber. The sensor exhibits a robust response of 45.2% R/R_0, with a sensitivity of 5.34 Ω/%RH, an adsorption time of 18 seconds, and a desorption time of 46 seconds. Additionally, the device demonstrates low hysteresis of 6.5% at 60%RH, with excellent repeatability and stability over 3.5 hours of continuous cycling. To showcase their potential for real-world applications, the printed sensors are integrated into a commercial KN95 mask for monitoring respiration parameters, such as respiration rate. This integration highlights the potential for future exploration in human health monitoring, utilizing fully printed, low-cost sensing devices.

In recent years, functional printing techniques have gained significant traction in the fabrication of cost-effective, flexible electronic devices and sensors. These approaches have enabled the development of straightforward, additively-manufactured sensor architectures, typically comprising an active sensing region coupled with metallic interdigitated electrodes (IDEs) for the measurement of parameters such as humidity[1], temperature[2], and strain[3]. Among these applications, the detection of relative humidity (%RH) has garnered considerable attention due to its relevance in a wide range of industries. Sectors with humidity-sensitive environments, such as precision agriculture[4], healthcare[5], and the transportation of high-value goods[6], are ideal candidates for the deployment of low-cost, single-use humidity sensors.

The fundamental operation of humidity sensors is predicated on the interaction between water molecules and the active sensing region, leading to changes in electrical properties that correlate with variations in %RH. Humidity sensors typically adopt resistive[7] or capacitive[8] sensing architectures, with less common designs incorporating calorimetric[9] or acoustic[10] principles. Resistive humidity sensors are particularly popular due to their simplicity, cost-effectiveness, and ease of integration with detection circuitry[11]. These sensors operate by detecting changes in the electrical resistance of a hygroscopic material, which occurs as a result of water molecule absorption, allowing for the quantification of %RH[12].

Over the years, various materials have been employed in resistive humidity sensors, including carbon-based nanomaterials, polymers, organic semiconductors, metal oxides, and ceramics[1,3,7,8,13,14]. While these materials offer good reproducibility and longevity, they are often constrained by narrow humidity operating ranges, slow response times, and susceptibility to harsh environmental conditions.

Wide bandgap semiconductors, such as ZnO (II-VI), GaN (III-V), and SiC (IV-IV), have emerged as promising candidates in the field of printed and flexible electronics[15–18]. In particular, SiC stands out due to its exceptional mechanical strength, chemical inertness, biocompatibility, thermal stability, and high electron mobility[19,20]. These properties render SiC suitable for long-term operation in corrosive, high-temperature, and oxidizing environments[21,22]. SiC has been explored for resistive humidity sensing applications in various forms, including crystalline wafers, nanowires, and nanocomposites[23–25]. Moreover, sophisticated fabrication techniques, such as direct growth and top-down/bottom-up approaches, have been utilized in

[1]Department of Electrical Engineering, École de Technologie Supérieure, 1100 Notre Dame Street West, Montréal, QC, H3C 1K3, Canada. [2]Department of Mechanical Engineering, Université du Québec à Trois-Rivières, 3351 Bd des Forges, Trois-Rivières, QC, G8Z 4M3, Canada.
✉e-mail: sylvaing.cloutier@etsmtl.ca

conjunction with transfer and conventional printing methods to produce complex and expensive devices[26].

To the best of our knowledge, SiC nanoparticles have not yet been employed in the fabrication of fully-printed humidity sensors, despite the successful production of SiC devices via other deposition and etching methods[27–31]. In this study, we develop a novel humidity sensor by formulating a low-cost active ink from commercial SiC nanoparticles. The material properties of this ink are comprehensively characterized using multiple techniques. We then fabricate a SiC-based humidity sensor by screen-printing the ink onto IDEs printed with commercial silver ink. Various SiC loadings and curing times are systematically investigated across a wide %RH range (10–90%) to optimize sensor performance, minimize hysteresis, and achieve rapid adsorption/desorption times. The sensing mechanism is thoroughly examined, and the fabricated devices are integrated into a commercial KN95 facemask to demonstrate their potential for respiratory monitoring applications.

Experimental section

Materials

Cubic Silicon Carbide (3C–SiC, beta phase, 99+%, 80 nm, cubic) nanoparticles were sourced from US Research Nanomaterials, Inc. (US2022). Flexible printed circuit (FPC) Kapton®, with a thickness of 0.005 inches, was obtained from American Durafilm. Loctite® EDAG 725A silver screen printing paste and Resin SOL725 were procured from Henkel. All materials were used as received without further modification.

Ink formulation and device fabrication

Precise quantities of 3C–SiC nanoparticles were mixed with the ink vehicle (SOL725) to achieve solid loading fractions of 20, 30, 40, and 50 wt%. The powder and ink vehicle were carefully weighed and combined, followed by thorough dispersion using a planetary mixer (Thinky Mixer Model AR-310). The mixing process involved 3 minutes of mixing and 3 minutes of degassing, for a total of 6 min, ensuring homogeneity and producing a stable dispersion with a shelf life exceeding 6 months. A total of 10 grams of ink was prepared for each formulation, as detailed in Table 1.

Table 1 | SiC humidity sensor ink formulations

Ink name	SiC nanoparticles (gms)	SOL725 (gms)
20-SiC	2	8
30-SiC	3	7
40-SiC	4	6
50-SiC	5	5

Commercial polyimide (Kapton®) substrates were prepared by cleaning with 99.9% pure acetone (Millipore Sigma 270725). Both the silver and SiC humidity sensing inks were printed using a 325-mesh stainless steel screen, yielding a wet film thickness of approximately 25.4 microns. The silver paste was printed onto the Kapton® substrate using a KEKO P250 automatic screen printer, following an interdigitated finger pattern with a trace width of 0.5 mm, trace spacing of 0.5 mm, and overall dimensions of 15 mm × 15 mm, as illustrated in Supplementary Fig. 1. The printed silver electrodes were cured in air at 300 °C for 60 min using a Manncorp (MC301N) reflow oven.

Subsequently, the active SiC-based ink was printed on top of the cured silver electrodes in a circular format with a diameter of 7.5 mm. The final sensor architecture was then cured in the reflow oven at 300 °C in air for 60, 120, and 180 min to investigate the effect of curing time on device performance. A schematic representation of the printing process is provided in Fig. 1a.

Characterization methods

Field emission scanning electron microscopy (FE-SEM) was conducted using a Hitachi SU8230 system equipped with a Bruker FlatQUAD EDS detector for elemental analysis. X-ray diffraction (XRD) patterns of the SiC nanopowder were acquired using an Anton Paar - XRDynamics 500 system with a Copper source. XRD spectra was analysed using the HighScore Plus software version: 4.6a and PDF-5+ ICDD database. Raman spectra was acquired using a WITec alpha300A Raman microspectroscopy system equipped with a 532 nm green laser. Ultraviolet-visible (UV-Vis) absorption spectra of the SiC powder were recorded using a Perkin-Elmer Lambda 750 spectrometer. Particle size of the SiC nanoparticles was measured using a Zetasizer Ultra Particle Size Analyzer (Malvern Panalytical) and via image processing using software Image J (version: 1.54g). Viscosity of the SiC inks was measured using a Anton Parr Physica MCR 501 viscometer with the 25 mm diameter spindle system.

X-ray photoelectron spectroscopy (XPS) was performed to analyze chemical bonding and oxidation states using an Escalab 250Xi (Thermo Fisher Scientific) system with a monochromated Al K_α source operating at 218.8 W. Thermogravimetric analysis (TGA) was performed to determine the curing temperature of the SiC ink using a Pyris Diamond TG/DTA

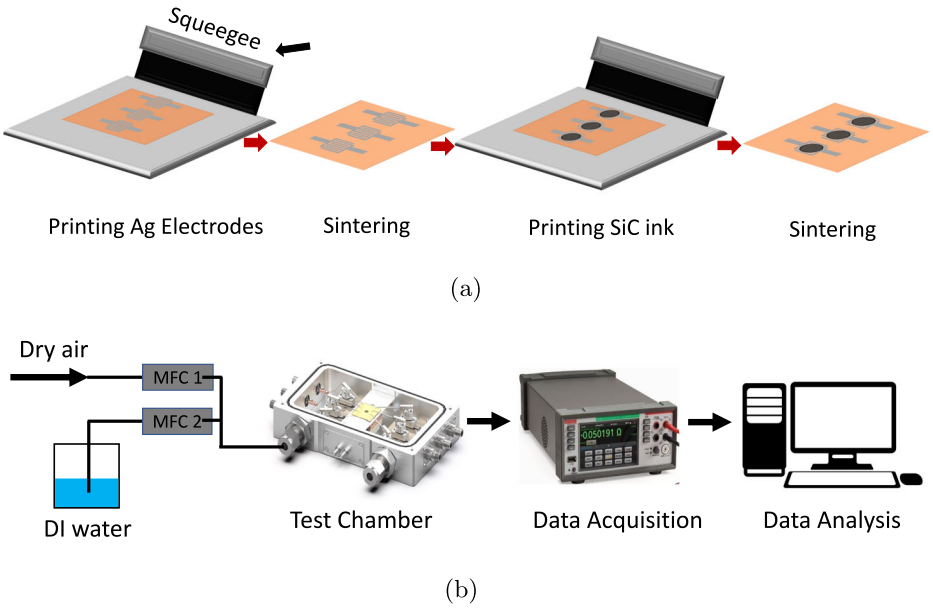

Fig. 1 | Schematic of sensor fabrication and humidity testing setup. a Schematic showing the screen printing process used to fabricate silver interdigitated electrodes followed by printing of the SiC humidity sensitive ink atop the electrodes (**b**) Schematic showing the test setup used to measure humidity sensor performance including the humidity test chamber with individual dry and wet gas mass flow controllers and the multi channel data acquisition unit.

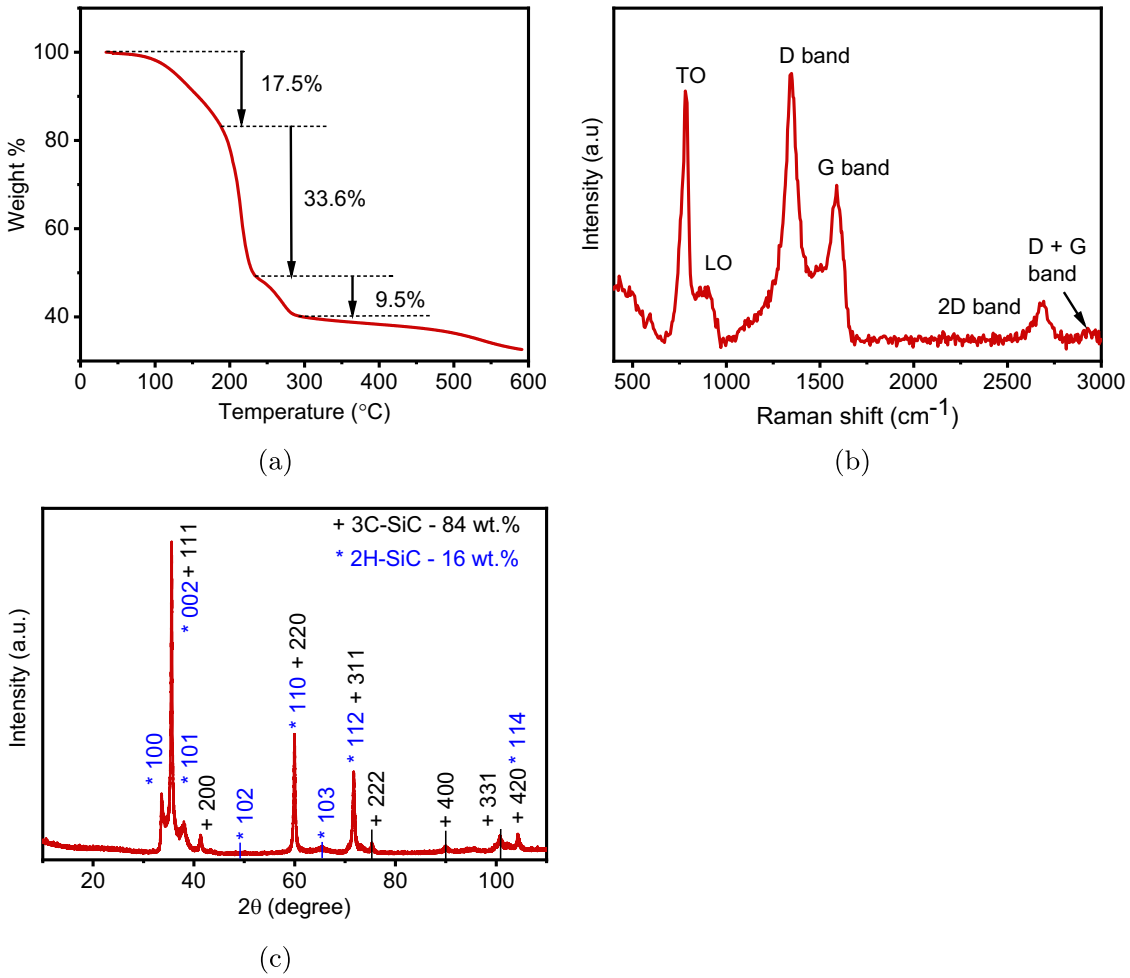

Fig. 2 | Characterization of the materials used to fabricate the SiC-based humidity-sensitive ink. a Thermogravimetric analysis (TGA) of the SOL725 resin conducted from room temperature to 600 °C, (**b**) Raman spectroscopy confirming the cubic crystalline phase of the SiC nanoparticles, and (**c**) X-ray diffraction spectra verifying the cubic phase along with the presence of a hexagonal phase in the as-received SiC nanoparticles.

system. Conductivity measurements of the printed SiC films were carried out using an Ossila T2001A3 four-point probe.

The humidity sensors were tested in a controlled humidity and temperature environment using a 6-channel micro-probe station (Nextron® MPS-PT6C). The two-wire resistance measurements were recorded via a 40-channel digital multimeter (Keithley 2790-L), as depicted in Fig. 1b. Current-voltage (I-V) characteristics of the thermistors were obtained using a Keithley DAQ6510 digital multimeter and a Keithley 2400 source-measure unit (SMU).

Custom MATLAB scripts were developed to process the raw data extracted from both the humidity test chamber and the digital multimeter. Breath monitoring experiments were conducted by the second author of this study, with protocols approved by the ethics review committee at ÉTS (No. H20231007). All experiments involving human subjects were performed in accordance with relevant guidelines and regulations.

Results and discussion

Material characterization and morphology

To optimize device performance, it is essential to ensure the complete removal of the polymeric resin (SOL725) from the printed films. Thermogravimetric analysis (TGA) of a 30 wt.% SiC and 70 wt.% SOL725 ink (Fig. 2a) was conducted between room temperature (23 °C) and 600 °C in air at a heating rate of 10 °C/min. The analysis shows a 17.5% reduction in sample weight between 30 °C and 200 °C, corresponding to the volatilization of high-volatility components in the ink vehicle. A further 33.6% weight reduction between 200 °C and 228 °C is attributed to the burning off of low-volatility components in the resin. An additional 9.5% reduction in weight is observed between 228 °C and 300 °C, which can be attributed to the removal of polymeric components, including surfactants and dispersants. The precise chemical composition of SOL725 was not disclosed by Henkel during this study. Beyond 300 °C, further weight reduction may result from the combustion of residual polymeric materials, potentially leading to carbonaceous deposits on the sensing film, which could negatively impact device performance. Consequently, 300 °C was identified as the optimal sintering temperature.

Raman spectra of the SiC powder (Fig. 2b) confirm its cubic crystal structure. Notable peaks were observed at 785, 897, 1346, 1588, 2684, and 2916 cm^{-1}. Peaks at 785 and 897 cm^{-1} correspond to the transverse and longitudinal optical modes of 3C–SiC, respectively[32]. The peak at 1346 cm^{-1} corresponds to the D band of carbon, while the 1588 cm^{-1} peak represents the G band associated with the A_{1g} vibrational mode of carbon[33]. The peaks at 2684 cm^{-1} and 2916 cm^{-1} correspond to the second-order D band (2D band) and the D+G band, respectively[34,35].

XRD patterns of the SiC particles (Fig. 2c) further validate its cubic crystalline structure, with distinct diffraction peaks observed. Peaks at 2θ = 35.6°, 41.4°, 59.9°, 71.7°, 75.4°, 89.9° and 104.4° correspond to the 111, 200, 220, 311, 222, 400, 331 and 420 crystal planes of the 3C–SiC structure, in line with ICDD card 04-008-2393. The presence of 2H – SiC peaks at 2θ = 33.6° (100), 35.5° (002), 38.1° (101), 49.7° (102), 60.1° (110), 65.5° (103), 71.8° (112) and 104.289° (114) (ICDD card 01-070-2550) suggests a blending of two phases during nanoparticle fabrication. To further investigate, default

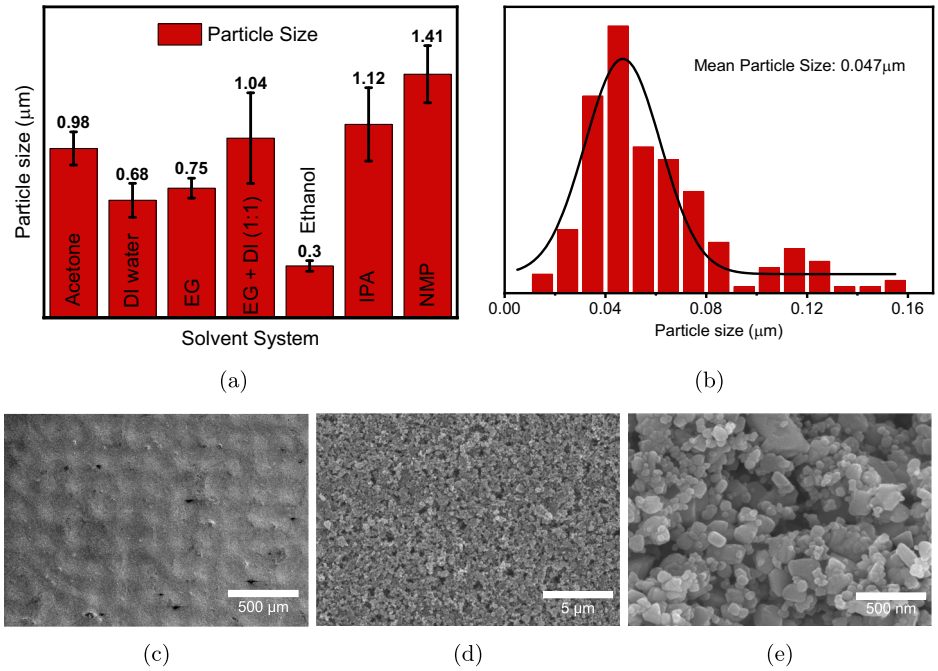

Fig. 3 | Morphological characterization of the SiC nanoparticles and printed SiC humidity-sensitive films. a Particle size distribution of SiC nanoparticles dispersed in various solvent systems; error bars represent the variability in measured particle size distribution for the corresponding solvents tested (**b**) particle size distribution determined through image processing analysis. Additionally, field emission scanning electron microscopy (FE-SEM) micrographs of the SiC humidity sensitive film cured at 300 °C are shown at magnifications of (**c**) 100×, (**d**) 10,000×, and (**e**) 100,000×.

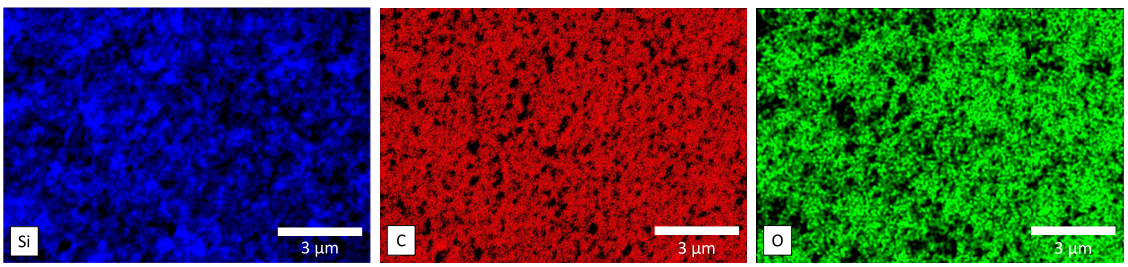

Fig. 4 | EDX elemental mapping of SiC film. Showing the spatial distribution of (**a**) Si, (**b**) C, and (**c**) O species within the printed SiC film, confirming the material's composition and the presence of native surface oxidation on the SiC nanoparticles.

Rietveld refinement was performed in HighScore Plus software, the Rietveld refinement spectra along with the relevant parameters are highlighted in Supplementary Fig. 2 and Supplementary Table 1. The analysis revealed that the SiC nanopowder comprises approximately 84 ± 1 wt.% of the 3C-SiC phase and 16 ± 4 wt.% of the 2H-SiC phase. It is important to note that accurate phase quantification was challenging due to peak overlap between the two phases.

A thorough investigation was conducted to determine the particle size distribution of the as-received SiC nanopowder. Following the methodology outlined by Nikkam et al.[36], we analyzed the particle size distribution of the SiC nanoparticles using dynamic light scattering (DLS) with various solvents, including acetone, deionized water (DI water), ethylene glycol (EG), a 1:1 blended ratio of DI water and EG, ethanol, isopropanol (IPA), and N-Methylpyrrolidone (NMP) (Fig. 3a). The DLS analysis revealed significant variability in the measured mean particle sizes, ranging from 1.41 μm in NMP to 0.3 μm in ethanol. This variation is likely due to different degrees of agglomeration or aggregation of the SiC nanoparticles within the various solvent systems. In addition to DLS, particle size distribution was further analyzed using the ImageJ software, where individual SiC particle diameters were measured from field emission scanning electron (FE-SEM) microscopy micrographs (Fig. 3b). The results indicate a wide distribution, with particle sizes ranging from 0.02 μm to 0.15 μm, yielding a mean particle size of 0.047 μm. This finding aligns with the manufacturer's reported specifications of 0.05–0.13 μm[37].

SiC-based humidity sensing films with 20, 30, 40, and 50 wt.% loadings were printed directly onto the prepared Kapton® substrates. The morphology and structure of the 40 wt.% SiC sensing film were analyzed via FE-SEM and energy dispersive X-ray analysis (EDX). As shown in Fig. 3c, the printed film is homogeneous, porous, and free of cracks. ASTM F2252 / F2252M-13e1 tests[38] confirmed excellent adhesion of the printed film to the Kapton® substrate. Further magnifications (Fig. 3d, e) reveal a densely packed network of SiC nanoparticles with intermittent pores. These pores facilitate the adsorption/desorption process, significantly improving the sensor's response times[1].

Elemental mapping (Fig. 4a, b, c) confirms a homogeneous distribution of Si and C elements, along with the presence of oxygen, indicating the formation of a native oxide layer on the SiC nanoparticles[19]. High resolution optical microscopy images as seen in Supplementary Fig. 3a and b, further validate the printed IDE and sensing film thickness. The silver ink achieved an average layer height of 12 μm, while the printed sensing film atop the IDEs reached 23 μm (Supplementary Fig. 3c and d).

The presence of functional groups on the surface of SiC nanoparticles, crucial to humidity sensing, was characterized by XPS analysis. The full XPS spectra (Fig. 5a) indicate the presence of silicon (Si_{2p}), carbon (C1s), and oxygen (O1s). Supplementary Table 2 shows that oxygen accounts for 30.8% of the atomic weight, likely due to oxygen-rich functional groups and silicon oxide formation. XPS spectra of individual species have been analyzed and presented in Supplementary Fig. 4.

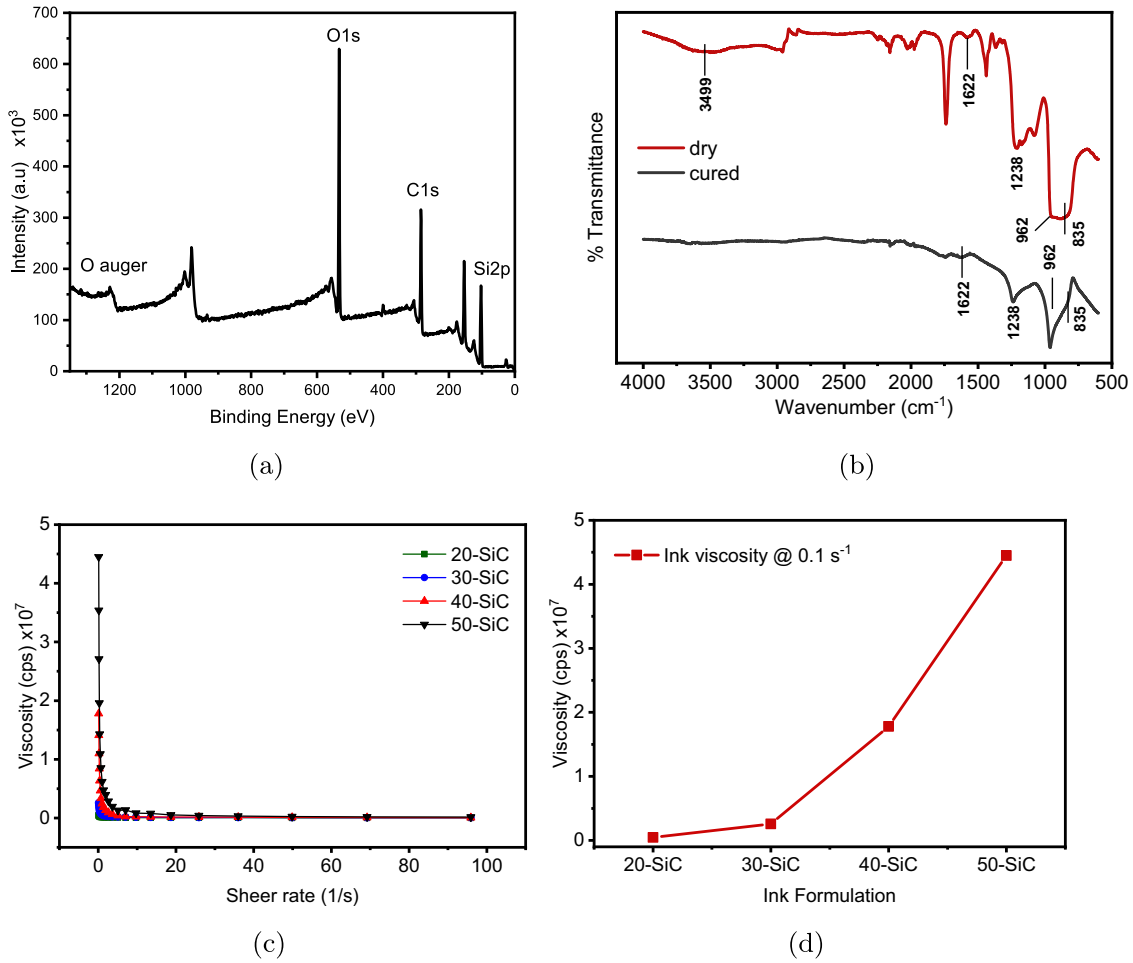

Fig. 5 | Characterization of printed SiC humidity-sensitive films: composition and rheological behavior. a X-ray photoelectron spectroscopy (XPS) spectra confirming the presence of Si, O, and C species in the printed films, (**b**) Fourier transform infrared (FTIR) spectra indicating the absence of hydrophilic -OH functional groups, (**c**) viscosity versus shear rate curves for 20, 30, 40, and 50 wt.% SiC-loaded humidity-sensitive inks, and (**d**) viscosity as a function of SiC weight percentage.

Deconvolution of the O1s peak (Supplementary Fig. 4a) revealed the presence of Si-O and C-O species at 533.5 eV. Similarly, deconvolution of the Si_2p peak (Supplementary Fig. 4b) identified peaks corresponding to Si–C, Si–CO, and Si – O_2, indicating an oxide layer formation during curing[19]. Analysis of the C1s peak (Supplementary Fig. 4c) revealed C–C, C – O, and O – C = O functional groups at 285, 287.2, and 289.8 eV, respectively[39]. Further calculations revealed that 29.2% of the oxygen species bond with silicon, while only 1.6% bond with carbon. The absence of C – OH bonding suggests a negligible amount of hydrophilic functional groups on the nanoparticle surface.

Fourier transform infrared (FTIR) spectroscopy was used to analyze the chemical structure of the SiC ink. Figure 5b compares the spectra of ink cured at 300 °C for 180 min with ink dried at 80 °C for 60 min. Both samples exhibited peaks at 835 cm^{-1} and 962 cm^{-1}, corresponding to Si–C and Si – O – Si stretching vibrational modes, respectively[40]. Peaks at 3499 cm^{-1} and 1622 cm^{-1} correspond to –OH stretching and bending modes, respectively, due to the physical adsorption of water vapor[19,41]. The absence of the 3499 cm^{-1} peak in the cured sample suggests the complete removal of hydroxyl groups from the SiC surface, whereas the 1622 cm^{-1} peak in the cured sample indicates minimal water vapor adsorption after fabrication. The lack of hydrophilic hydroxyl groups on the SiC surface likely impedes the adsorption and ionization of water molecules, limiting the flow of charge carriers across a broad %RH range. We hypothesize that the device's performance is driven by a swelling mechanism, resulting in a positive resistance change with increasing relative humidity[42].

Viscosity is a key parameter in optimizing the flow characteristics of screen-printable inks, typically ranging between 1×10^3 to 2×10^7 centipoise (cps) according to IPC standards[43]. Figure 5c illustrates the viscosity behavior of 20, 30, 40, and 50 wt.% SiC-loaded inks over a shear rate range of 0.1–100 (1/*s*) at room temperature. As the SiC loading increases, a significant rise in viscosity is observed, particularly between the 30 wt.% and 50 wt.% inks at a shear rate of 0.1 (1/*s*) (Fig. 5d). The viscosity of the 40 wt.% SiC ink reaches 1.78×10^7 cps at a shear rate of 0.1 (1/*s*), which is near the upper limit for screen-printable inks. However, the viscosity of the 50 wt.% ink increases to 4.75×10^7 cps, rendering it unsuitable for screen printing applications.

We next investigated the electronic properties of SiC sensor films with 20, 30, 40, and 50 wt.% particle loading, cured at 300 °C for durations of 60, 120, and 180 minutes. Electrical conductivity was measured using the four-point probe method at ambient temperature and humidity for five printed samples per test condition. As shown in Fig. 6a and Supplementary Table 3, SiC inks with 30 wt.% and 40 wt.% particle loading cured for 180 min exhibited the highest electrical conductivities, reaching values of $3.09 \pm 3 \times 10^{-4}$ and $1.52 \pm 1 \times 10^{-2}$ S/m, respectively. Figure 6b presents the current-voltage (I-V) characteristics of the printed humidity sensing films. The observed linear ohmic behavior between -5 V and +5 V indicates that the device functions as a resistor, where the current is directly proportional to the applied voltage[44].

Baseline resistance values for all printed inks were recorded under ambient conditions of temperature and humidity, with the data provided in

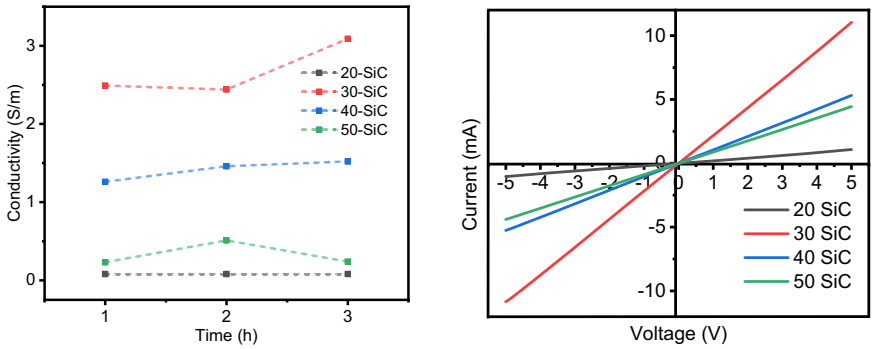

Fig. 6 | Electrical and I–V characteristics of printed SiC humidity-sensitive films. a Electrical conductivity measurements of 20, 30, 40, and 50 wt.% SiC-loaded films as a function of curing time, and (**b**) current-voltage (I-V) characteristics of the printed SiC humidity-sensitive films.

Supplementary Table 4. Films loaded with 20 wt.% particles exhibited minimal changes in baseline resistance across all three curing cycles. In contrast, the 50 wt.% loaded samples displayed the highest baseline resistance, with notable inconsistencies likely due to poor printability due to its high viscosity as previously discussed. For the 30 wt.% loaded samples, a 47.5% reduction in baseline resistance was observed between 60 and 180 minutes of curing, from 582 ± 8 Ω to 306 ± 30 Ω. Similarly, the 40 wt.% samples exhibited a 33.5% reduction from 1078 ± 19 Ω to 717 ± 19 Ω. These reductions in baseline resistance can be attributed to film densification with increasing curing time[45–47]. These results indicate that films cured at 300 °C for 180 min offer optimal performance for humidity sensors. It is noteworthy that the 30 wt.% samples exhibited lower overall baseline resistance compared to the 40 wt.% loadings.

Figure 7 a demonstrates the humidity sensing performance of printed sensors with varying SiC loadings after curing for 180 min. Each concentration was tested with three samples, each cycled five times between 10–90% RH at a constant temperature of 25 °C. As expected, all devices showed increased electrical resistance with rising relative humidity (%RH), a behavior attributed to the swelling mechanism[39], which will be further elaborated in the subsequent section. Table 2 provides the evolution of the electrical response (R/R_0) for the humidity sensors across different loading concentrations and curing times. The humidity sensor response was calculated using Equation (1)[48]:

$$\%(R/R_0) = \frac{R_{90} - R_{10}}{R_{10}} \times 100\% \quad (1)$$

where R represents the electrical resistance at 10% and 90% RH. Notably, the 40 wt.% loaded SiC ink cured for 180 min demonstrated a response of 45.2 ± 5.71% (R/R_0), which was calculated using Eq. (1) over the tested humidity range. Conversely, the 20 wt.% loaded sensor exhibited consistent response across all curing times, suggesting that the particle densification process was complete after 60 minutes of curing. The 50 wt.% loading, however, resulted in a decrease in response, likely due to film cracking and disruption of conductive pathways. These findings are consistent with the observed changes in electrical conductivity and baseline resistance. The 30 wt.% and 40 wt.% loaded films showed enhanced response and sensitivity with longer curing times, corresponding with their electrical properties.

Device sensitivity (S) and hysteresis (H) are calculated as per equations (2) and (3) respectively.

$$S = \frac{R_{90} - R_{10}}{\Delta RH} \quad (2)$$

$$H = \frac{\Delta H_{max}}{S} \quad (3)$$

The sensitivity of the 40 wt.% SiC sensor was determined to be 5.34 ± 0.6 Ω/%RH, with a maximum hysteresis of 6.5% RH at 60% RH. Further characterization of the 40 wt.% SiC ink is shown in Fig. 7b, which illustrates the adsorption and desorption behavior between 10–90% RH. The sensor followed a second-order polynomial fit governed by Equation (4), with an R^2 coefficient of 0.99, as depicted in Fig. 7c.

$$Y = -2.0 \times 10^{-5} X^2 + 8.1 \times 10^{-3} X + 0.9384 \quad (4)$$

The adsorption and desorption time constants (response and recovery times) are crucial in assessing how quickly a sensor can detect changes in relative humidity. The test procedure is summarized in Supplementary Fig. 5. Upon water drop deposition, Fig. 7d shows a rapid increase in device response until saturation, followed by a sharp drop in response after water removal, eventually returning to the baseline state. Since this test was conducted under ambient conditions, the %RH ranged between 40% (ambient humidity) and 100% (water saturation). The measured adsorption and desorption times were 18 s and 46 s, respectively. These time constants are consistent with other recently reported printed humidity sensors[23,25,39].

We evaluated the reproducibility of the humidity sensor responses through rapid cycling at the maximum permissible speed of the test chamber, within a limited testing range of 30–70% RH, as shown in Fig. 7e. The sensors exhibit minimal variability, with only a slight drift in baseline resistance during the initial cycles. This drift can be tentatively attributed to the relaxation of the porous SiC particle network as the RH changes. Long-term reliability was also assessed by cycling the sensors over extended periods. Initially, the sensors were cycled five times between 10–90% RH over 3.5 hours, as presented in Fig. 7f. The sensors responded consistently to the RH variations, indicating excellent long-term cycling stability. Moreover, the sensors demonstrated the ability to detect small variations in RH (≤ 4%), occurring as the test chamber stabilized at each point. Remarkably, response changes as small as 0.003% (R/R_0) were successfully recorded, as illustrated in Fig. 7g. In a separate experiment (Fig. 7h), the sensors were subjected to incremental changes in humidity from 10–90% RH, with 10% RH steps and a stabilization period of 15 minutes between each step. The sensors maintained stable performance with only a slight baseline resistance drift (4%) after the cycling was completed. The temperature dependence of the sensor, measured between 25 °C and 50 °C at a constant 40% RH, is depicted in Fig. 7i. The three devices tested exhibited a small negative temperature coefficient of resistance (NTCR) of $-0.005\ \Omega°C^{-1}$, which is likely due to increased charge carrier hopping between neighboring SiC nanoparticles as the temperature rises[49]. Notably, the SiC humidity sensors display a positive resistance change with increasing RH and a negative resistance change with rising temperature. However, the small NTCR suggests that temperature has a limited impact on overall sensor performance.

For a comparative analysis, the characteristics of recently reported (1) printed resistive humidity sensors and (2) SiC-based humidity sensors are summarized in Table 3. It is worth noting that no prior studies on fully screen-printed SiC humidity sensors were found. Our SiC humidity sensors

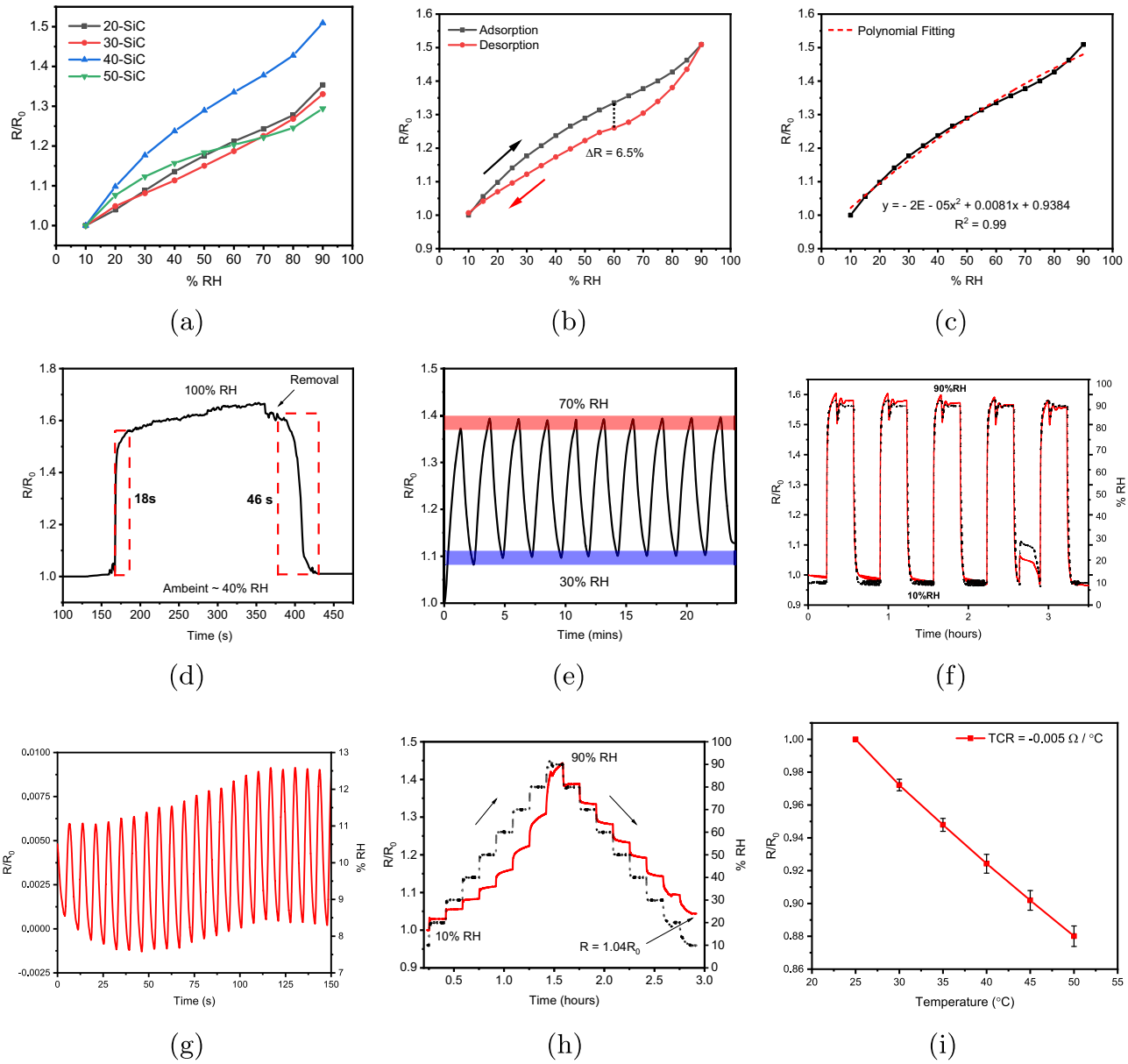

Fig. 7 | Performance and reliability evaluation of printed SiC-based humidity sensors. a Response of 20, 30, 40, and 50 wt.% SiC humidity sensors cured at 300 °C for 180 minutes. Performance of the 40 wt.% SiC sensors: (**b**) adsorption/desorption plot showing a hysteresis of 6.5% at 60% RH, (**c**) response curve with polynomial fitting, (**d**) plot determining adsorption/desorption time constants via a drop test, (**e**) high-speed cycling of the SiC humidity sensor between 30–70% RH, (**f**) long-term cycling between 10–90% RH over a 3.5 h period, (**g**) detection of minute variations in %RH using the 40 wt.% printed SiC humidity sensor, (**h**) long-term cycling between 10–90% RH in 10% RH increments, and (**i**) temperature coefficient of resistance measured at different temperatures.

represent a significant advancement over existing devices by utilizing commercially available SiC nanoparticles and a standardized ink vehicle, addressing challenges related to material availability, cost, and consistency. In contrast to complex, energy-intensive methods like PECVD, we employ screen printing, offering faster production, greater design flexibility, and reduced material consumption. This scalable and cost-effective fabrication technique enables broader application of SiC-based humidity sensors. Although some solid-state devices offer comparable or superior performance and response times[50], their high material costs and fabrication complexities limit their suitability for large-scale applications[51]. Table 3 also highlights SiC humidity sensors fabricated through more intricate processes such as chemical vapor deposition or SiC nanowire networks. These nanowire-based sensors offer higher aspect ratios and an increased number of contact points compared to nanoparticle-based devices, potentially leading to higher responses, while a well-dispersed porous SiC network enables faster adsorption and desorption times. However, the fabrication techniques used for these sensors significantly increase processing costs. In contrast, our screen-printed SiC nanoparticle-based devices provide sufficient performance for many applications, while being produced at a much lower cost using manufacturing-grade equipment.

Table 2 | Humidity sensor response (% change in resistance R/R_0) over different SiC loadings and cure temperatures

Time (h)	20-SiC R/R_0	30-SiC	40-SiC	50-SiC
1	31.65 ± 1.43	18.48 ± 1.60	28.75 ± 1.80	41.70 ± 3.88
2	31.85 ± 2.89	22 ± 1.68	37.65 ± 4	35.50 ± 3.15
3	29.31 ± 3.16	28.75 ± 3	45.20 ± 5.71	30.72 ± 4.73

Table 3 | Comparison of sensing performance of recently reported humidity senors

Material	Fabrication	Device Type	Testing Range (%RH)	Response (R/R_0)	Adsorption/ desportion time	Ref
Printed resistive humidity sensors						
CNF/CB/TX-100	screen printing	resistive	30–90	120%	10s / 6s	1
daily carbon ink	paint brush	resistive	0–95	178.7%	56s / 14s	39
Graphene	CVD	resistive	10–90	1.2%	0.6 / 0.4	77
MWCNT/polyimide	in-situ polymerization	resistive	20–90	12.8%	5s / 600s	78
RGO/PDDA	layered self-assembly	resistive	11–97	37.4%	108s / 94s	79
PEG / gold nano particles	inkjet printing	resistive	1.8–95	10^4	1.2s / 3s	80
PHEMA	gravure printing	resistive	30–80	172%	-	81
MWCNT w/ integrated printed heater	screen printing	resistive	10–90	55%	4.6 min / 30.9 min	82
Graphene/methyl red	inkjet printing	resistive	5–95	96.36	0.251s / 0.35s	83
polyDADMAC	direct write printing	resistive	10–90	> 99%	7s / 213s	84
Reported SiC humidity sensors						
SiC 2D nanosheets	spin coating	resistive	11–95	-	3s / 3s	19
SiC on p – Si wafer	PECVD	capacitive	10–90	200%	3 min / 4 min	85
SiC nanopaper	SiC nanowire compression	resistive	30–65	90%	41s / 124s	23
SiC nanowires on nanoporous Si pillar array	CVD + etching	capacitive	11–95	960%	105s / 85s	25
SiC nano particle ink	screen printing	resistive	10–90	45.2%	18s / 46s	This work

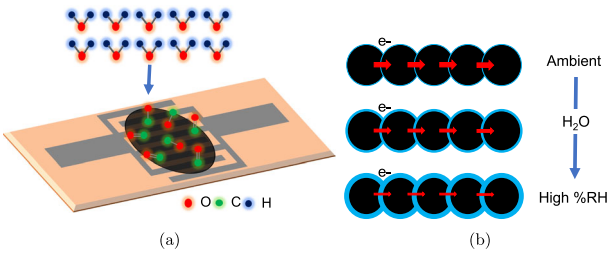

Fig. 8 | Humidity sensing mechanism of SiC film: water adsorption and charge carrier mobility reduction. a Schematic illustrating the adsorption of water molecules onto the SiC humidity sensor film, and (**b**) the reduction in charge carrier mobility with increasing %RH.

Humidity sensing mechanism

The responsivity of resistance-type humidity sensors is primarily driven by the adsorption and desorption of water molecules by the sensing material[52]. A negative resistance change with increasing RH can generally be attributed to the presence of hydrophilic functional groups, such as –OH, C = O, and C – O, which promote water molecule attachment to the sensing film surface[19]. This leads to ionization and the production of hydronium ions (H_3O^+)[53], facilitating proton movement and thereby reducing resistance through proton hopping in the Grotthuss chain reaction[54]. Conversely, positive resistance change in humidity-sensitive materials typically results from swelling of the sensing film as it absorbs water molecules[55–59]. In our case, the printed SiC humidity sensing films exhibit a positive resistance change with increasing RH. This can be further elucidated through XPS and FTIR measurements, as shown in Fig. 5. XPS analysis of the SiC thermistor films reveals that only 1.6% of atomic oxygen is bonded to carbon, forming C – O and O – C = O hydrophilic groups. The results also confirm the formation of a silicon oxide shell around the SiC particles, with 8.1% and 11.8% atomic oxygen bonded to silicon atoms forming Si–CO and Si – O_2 species, respectively. Silicon dioxide (SiO_2) is known for its strong hydrophilic properties[60] due to the presence of hydroxyl (–OH) groups on its surface, which is why it is often used to enhance humidity sensing performance[58,61–63]. However, FTIR measurements (Fig. 5b) confirm that all –OH groups are removed from the sensing film after curing at 300 °C.

Figure 8 presents a schematic illustration of the adsorption mechanism of water molecules onto printed SiC films. Under dry conditions, the electrical resistance of SiC remains minimal, as electron transport is facilitated by tunneling between the nanoparticles[64]. The porous nature of the SiC nanoparticle film offers a high surface-to-volume ratio, allowing significant adsorption of water molecules via capillary condensation[65]. As the relative humidity (%RH) increases, water molecules infiltrate the film's pores, eventually reaching equilibrium. The accumulation of adsorbed water leads to the formation of a water film around the SiC nanoparticles, thereby impeding the electron tunneling process[39]. Consequently, the device exhibits higher electrical resistance at elevated %RH levels. It is important to note that deionized (DI) water, with its low electrical conductivity (approximately 1–5 μS/m)[66], was employed in these experiments. While a small fraction of water molecules may dissociate to form hydronium ions, potentially enhancing electron conduction, this contribution is expected to be negligible and unlikely to significantly impact the sensing mechanism.

Device integration

Due to their remarkable sensitivity and rapid response, the printed SiC humidity sensors demonstrate potential for a broad spectrum of applications. Prior research has shown that tracking variations in relative humidity (%RH) during breathing cycles can provide access to critical respiratory parameters, aiding in preventative healthcare for patients[67]. In this study, we selected a KN95 mask for integrating flexible printed SiC sensors to monitor breath, as illustrated in Fig. 9. The sensor arrays were fabricated using an optimized 40%-loaded SiC ink formulation, cured at 300 °C for 180 min. These arrays were affixed to the exterior surface of the mask, as depicted in Fig. 9c.

A simple experiment was conducted wherein a subject breathed normally for 60 seconds, followed by 10 deep respirations. Resistance values were recorded at one-second intervals, as shown in Fig. 9a. Owing to the rapid adsorption and desorption response of the printed sensors, distinct variations in sensor output were observed between normal and deep breathing cycles. The data acquired from such trials hold the potential for

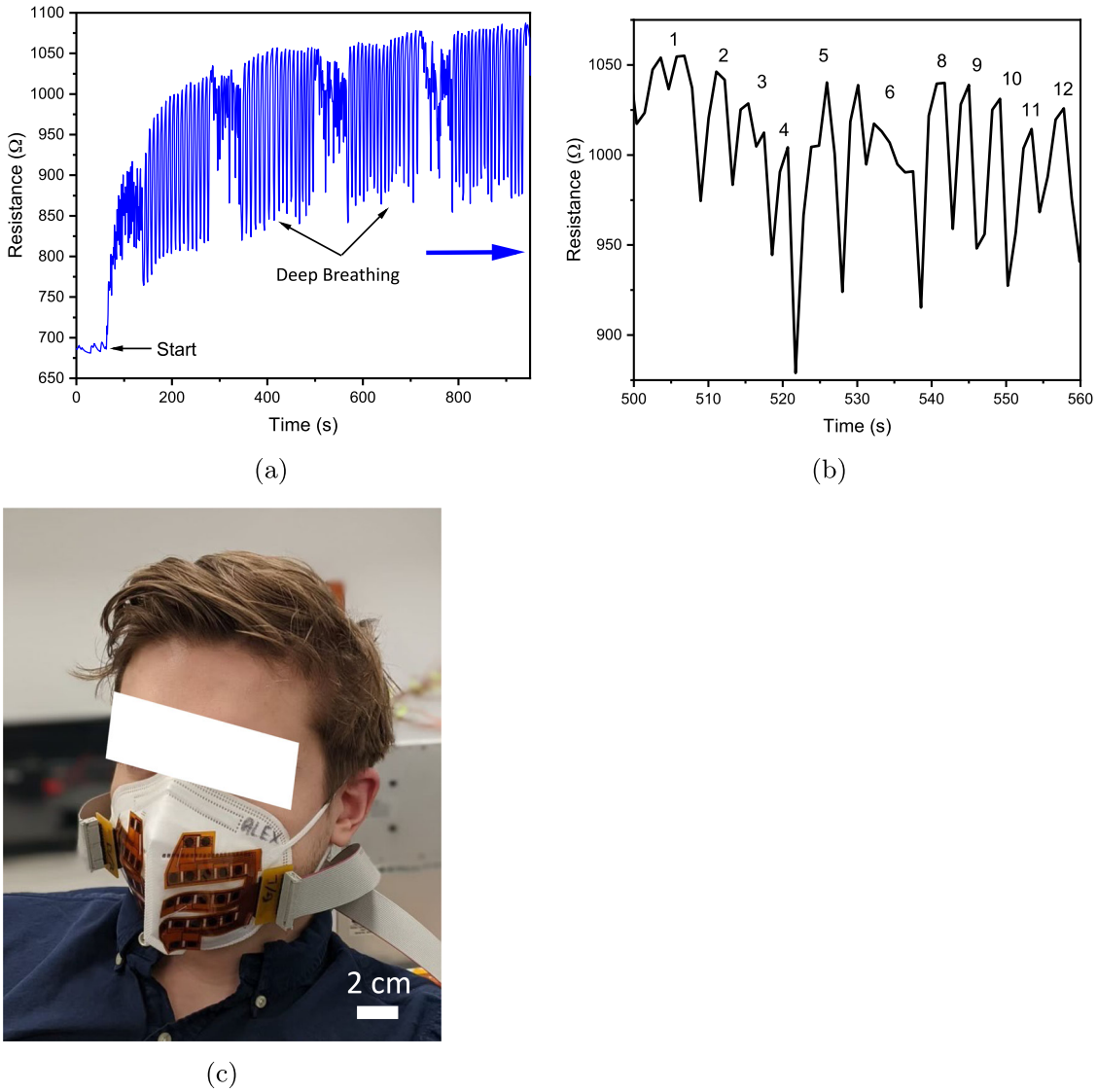

Fig. 9 | Printed SiC humidity sensors for breath monitoring and respiration rate detection. a Sensor response during human breathing with SiC humidity sensors attached to the exterior of a KN95 mask, (**b**) determination of human respiration rate based on the sensor response, and (**c**) photograph of the breath monitoring setup used for the measurements.

extracting physiological parameters related to respiratory rate, monitoring of chronic obstructive pulmonary diseases (COPD), asthma, and sleep apnea[67–70]. For instance, Fig. 9b displays the change in %RH over a 60 s period, corresponding to 12 response cycles, which aligns with a normal and healthy respiration rate[71]. Additionally, a baseline shift in sensor resistance was noted throughout the test duration. Since the sensors were placed on the exterior of the mask, this baseline shift may be indicative of humidity saturation or potential clogging of the KN95 mask.

These humidity sensor arrays can also be employed to assess humidity distribution across a surface, as demonstrated in Fig. 10a. Figure 10b illustrates a matrix of 18 sensors, with a hand placed over the sensors both with and without a glove. A rise in resistance is observed when the bare hand approaches the sensors, attributed to the moisture from the skin. In contrast, no change in sensor response occurs when the hand with a glove is placed near the sensor array. Figure 10c captures the transient resistance behavior in proximity to the bare hand and the recovery when exposed to hot air after the hand is removed. This highlights the potential for mapping humidity changes across large areas, which is valuable for applications such as leak and flood detection[72].

This study demonstrates that the printed SiC humidity sensors exhibit high sensitivity and reproducibility. Furthermore, the chemical inertness and biocompatibility of both Kapton and SiC[73–76] suggest these sensors could be effectively utilized in moisture detection within critical environments such as medical facilities, refineries, and greenhouses. Notably, the relatively low cost of silver ink, the Kapton substrate, and SiC powder makes these sensors ideal candidates for low-cost, high-volume applications[50].

Conclusion

This study presents a high-performance humidity sensor based on a screen-printable SiC nanoparticle ink formulation. The simplicity of the device architecture, use of commercially available low-cost materials, and biocompatibility make these sensors applicable across a broad range of fields. Various SiC loadings and curing temperatures were evaluated, with the optimal performance observed at a 40 wt.% SiC particle loading and curing at 300 °C for 180 min. Under these conditions, the sensor achieved a response of 45.2 ± 5.7% (R/R_0) between 10% RH and 90% RH, with fast adsorption and desorption times of 18 s and 46 s, respectively.

These humidity sensors exhibit an increase in electrical resistance with rising %RH, primarily due to physical swelling, as the absence of hydrophilic –OH groups limits water absorption. The sensor's response follows a second-order polynomial fit to %RH changes, with a high correlation coefficient ($R^2 = 0.99$). Additionally, the sensor demonstrated excellent

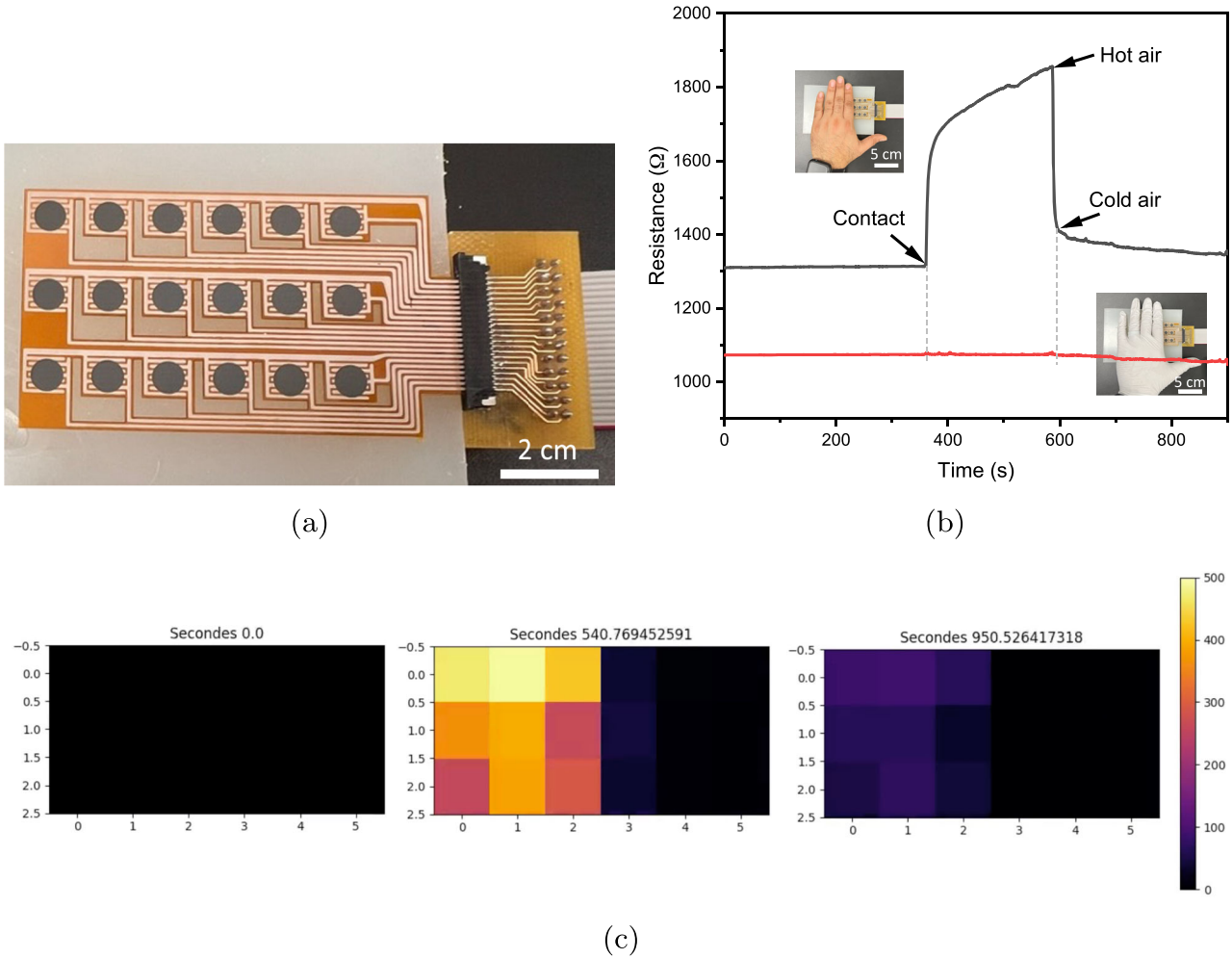

Fig. 10 | Printed SiC sensor array for large-area humidity mapping and human interaction detection. a Implementation of a 6 × 3 array of SiC humidity sensors, (**b**) demonstration of the change in response of the printed SiC humidity sensor array with contact from human hand with and without a glove (barrier), (**c**) illustrating depicting the change in response where the image at O seconds corresponds to the sensor arrays response at rest. The second image reflects sensor behavior at 540 s where sensors that are in contact with the uncovered hand detect a change in humidity. The last iamge corresponds to the sensor arrays response at 950 s where sensors that responded to change in humidity show a very small residual resistance value after desorption.

thermal stability, exhibiting a low temperature coefficient of resistance (TCR) of −0.005 Ω/°C. After prolonged exposure at various humidity levels, the baseline resistance showed minimal drift, with only a 4% change over three hours.

As a proof-of-concept, we demonstrated the potential application of these printed humidity sensors for monitoring human respiration within a KN95 mask. Moreover, the sensors were implemented in a matrix configuration to detect skin contact. Due to their high performance, fast response times, and stability, these sensors hold promise for critical applications in environments such as chemical storage, food production, agriculture, and flood detection.

Data availability

The authors verify that the data backing the study's conclusions can be found in the article. The raw data supporting the study's findings can be obtained from the corresponding author, S.G.C., upon reasonable request.

Code availability

The authors verify that the Matlab codes for data processing can be obtained from the corresponding author, S.G.C., upon reasonable request.

Received: 30 March 2024; Accepted: 29 April 2025;
Published online: 27 May 2025

References

1. Tachibana, S. et al. A Printed Flexible Humidity Sensor with High Sensitivity and Fast Response Using a Cellulose Nanofiber/Carbon Black Composite. *ACS Appl. Mater. Interf.***14**, 5721–5728 (2022).
2. Fourmont, P., Bai, Y., Fortier, F.-X. & Cloutier, S. G. Graphene-Enhanced Screen-Printed BiFeO3-Based Thermistors. *ACS Appl. Electron. Mater.* **4**, 5905–5913 (2022).
3. Wang, Y.-F. et al. Fully Printed PEDOT:PSS-based Temperature Sensor with High Humidity Stability for Wireless Healthcare Monitoring. *Sci. Rep.* **10**, 2467 (2020).
4. Imam, S. A., Choudhary, A. & Sachan, V. K. Design issues for wireless sensor networks and smart humidity sensors for precision agriculture: A review. In *2015 International Conference on Soft Computing Techniques and Implementations (ICSCTI)*, 181–187 (2015).
5. Barmpakos, D., Segkos, A., Tsamis, C. & Kaltsas, G. A disposable flexible humidity sensor directly printed on paper for medical applications. *J. Phys.: Conf. Ser.* **931**, 012003 (2017).
6. Wen, N. et al. Emerging flexible sensors based on nanomaterials: recent status and applications. *J. Mater. Chem. A* **8**, 25499–25527 (2020).
7. Zhang, X. et al. Novel Printed Carbon Nanotubes Based Resistive Humidity Sensors. *2019 IEEE International Conference on Flexible and Printable Sensors and Systems (FLEPS)* 1–3 https://ieeexplore.

ieee.org/document/8792298/ (2019). Conference Name: 2019 IEEE International Conference on Flexible and Printable Sensors and Systems (FLEPS) ISBN: 9781538693049 Place: Glasgow, United Kingdom Publisher: IEEE.
8. Komazaki, Y. & Uemura, S. Stretchable, printable, and tunable PDMS-CaCl2 microcomposite for capacitive humidity sensors on textiles. *Sens. Actuators B: Chem.* **297**, 126711 (2019).
9. Soga, T., Jimbo, Y., Suzuki, K. & Citterio, D. Inkjet-Printed Paper-Based Colorimetric Sensor Array for the Discrimination of Volatile Primary Amines. *Anal. Chem.* **85**, 8973–8978 (2013).
10. Caliendo, C. et al. Surface acoustic wave humidity sensor. *Sens. Actuators B: Chem.* **16**, 288–292 (1993).
11. Lu, Y. et al. Highly stable Pd/HNb 3 O 8-based flexible humidity sensor for perdurable wireless wearable applications. *Nanoscale Horiz.* **6**, 260–270 (2021).
12. Farahani, H., Wagiran, R. & Hamidon, M. N. Humidity Sensors Principle, Mechanism, and Fabrication Technologies: A Comprehensive Review. *Sens. (Basel, Switz.)* **14**, 7881–7939 (2014).
13. Dubey, C. & Kumar, B. Organic Humidity Sensors with Different Materials and Its Application in Environment Monitoring. In *2018 5th IEEE Uttar Pradesh Section International Conference on Electrical, Electronics and Computer Engineering (UPCON)*, 1–6 https://ieeexplore.ieee.org/abstract/document/8597009 (2018).
14. Jeong, H., Noh, Y. & Lee, D. Highly stable and sensitive resistive flexible humidity sensors by means of roll-to-roll printed electrodes and flower-like TiO2 nanostructures. *Ceram. Int.* **45**, 985–992 (2019).
15. Syed, N. et al. Printing two-dimensional gallium phosphate out of liquid metal. *Nat. Commun.* **9**, 3618 (2018).
16. Arrabito, G. et al. Printing ZnO Inks: From Principles to Devices. *Crystals* **10**, 449 (2020).
17. Dong, H., Liu, W., Li, Y., Chen, X. & Wang, D. Fully Printed Flexible Zinc Oxide Patch for Wearable UV Light Sensing. *Adv. Electron. Mater.* **9**, 2300469 (2023).
18. Lerner, R. et al. Heterogeneous Integration of Microscale Gallium Nitride Transistors by Micro-Transfer-Printing. In *2016 IEEE 66th Electronic Components and Technology Conference (ECTC)*, 1186–1189 https://ieeexplore.ieee.org/abstract/document/7545575?casa_token=2wTRziVQORUAAAAA:HA6un8NMEF3uT--SnRk5sbL4NZY2cap-vmSl-J_ETQ2u2yt2HW3PbxKdc300DOu-hTBCc6I (2016).
19. Sun, L., Wang, B. & Wang, Y. A Novel Silicon Carbide Nanosheet for High-Performance Humidity Sensor. *Adv. Mater. Interfaces* **5**, 1701300 (2018).
20. Sun, L., Han, C., Wu, N., Wang, B. & Wang, Y. High temperature gas sensing performances of silicon carbide nanosheets with an n-p conductivity transition. *RSC Adv.* **8**, 13697–13707 (2018).
21. Müller, G., Krötz, G. & Niemann, E. SiC for sensors and high-temperature electronics. *Sens. Actuators A: Phys.* **43**, 259–268 (1994).
22. Phan, H.-P. et al. Piezoresistive effect in p-type 3C-SiC at high temperatures characterized using Joule heating. *Sci. Rep.* **6**, 28499 (2016).
23. Li, G.-y et al. Room-Temperature Humidity-Sensing Performance of SiC Nanopaper. *ACS Appl. Mater. Interfaces* **6**, 22673–22679 (2014).
24. Ahmed, H., Abduljalil, H. M. & Hashim, A. Analysis of Structural, Optical and Electronic Properties of Polymeric Nanocomposites/ Silicon Carbide for Humidity Sensors. *Trans. Electr. Electron. Mater.* **20**, 206–217 (2019).
25. Wang, H. Y., Wang, Y. Q., Hu, Q. F. & Li, X. J. Capacitive humidity sensing properties of SiC nanowires grown on silicon nanoporous pillar array. *Sens. Actuators B: Chem.* **166-167**, 451–456 (2012).
26. Nguyen, N.-K. et al. Wide-Band-Gap Semiconductors for Biointegrated Electronics: Recent Advances and Future Directions. *ACS Appl. Electron. Mater.* **3**, 1959–1981 (2021).
27. Mott, M. & Evans, J. R. G. Solid Freeforming of Silicon Carbide by Inkjet Printing Using a Polymeric Precursor. *J. Am. Ceram. Soc.* **84**, 307–13 (2004).
28. Terrani, K. A. et al. Irradiation stability and thermomechanical properties of 3D-printed SiC. *J. Nucl. Mater.* **551**, 152980 (2021).
29. Zhou, N. et al. Stereolithographically 3D Printed SiC Metastructure for Ultrabroadband and High Temperature Microwave Absorption. *Adv. Mater. Technol.* **8**, 2201222 (2023).
30. Gómez-Gómez, A. et al. Highly-porous hierarchical SiC structures obtained by filament printing and partial sintering. *J. Eur. Ceram. Soc.* **39**, 688–695 (2019).
31. Chen, H. et al. 3D printing of SiC ceramic: Direct ink writing with a solution of preceramic polymers. *J. Eur. Ceram. Soc.* **38**, 5294–5300 (2018).
32. Lebedev, A. A., Oganesyan, G. A., Kozlovski, V. V., Eliseyev, I. A. & Bulat, P. V. Radiation Defects in Heterostructures 3C-SiC/4H-SiC. *Crystals* **9**, 115 (2019).
33. Hsu, C.-H., Cloutier, S. G., Palefsky, S. & Xu, J. Synthesis of Diamond Nanowires Using Atmospheric-Pressure Chemical Vapor Deposition. *Nano Lett.* **10**, 3272–3276 (2010).
34. Dragomir, M., Valant, M., Fanetti, M. & Mozharivskyj, Y. A facile chemical method for the synthesis of 3C-SiC nanoflakes. *RSC Adv.* **6**, 21795–21801 (2016).
35. Zhu, K. et al. Graphene covered SiC powder as advanced photocatalytic material. *Appl. Phys. Lett.* **100**, 023113 (2012).
36. Nikkam, N. et al. Fabrication, characterization and thermophysical property evaluation of sic nanofluids for heat transfer applications. *Nano-Micro Lett.* **6**, 178–189 (2014).
37. Silicon Carbide SiC Nanopowder / Nanoparticles (SiC, beta, 99+%, <80 nm, cubic). https://www.us-nano.com/inc/sdetail/373.
38. ASTM F2252/F2252M-13e1 - Standard Practice for Evaluating Ink or Coating Adhesion to Flexible Packaging Materials Using Tape. https://webstore.ansi.org/standards/astm/astmf2252f2252m13e1.
39. Duan, Z. et al. Daily writing carbon ink: Novel application on humidity sensor with wide detection range, low detection limit and high detection resolution. *Sens. Actuators B: Chem.* **339**, 129884 (2021).
40. Jiang, S. et al. Study on the synthesis of β-SiC nanoparticles from diamond-wire silicon cutting waste. *RSC Adv.* **9**, 23785–23790 (2019).
41. Luo, G. et al. Study on Rheological Behavior of Micro/Nano-Silicon Carbide Particles in Ethanol by Selecting Efficient Dispersants. *Materials* **13**, 1496 (2020).
42. Montes-García, V. & Samorì, P. Humidity Sensing with Supramolecular Nanostructures. *Adv. Mater.* **36**, 2208766-17 (2024).
43. Screen making for printed electronics- specification and tolerancing. https://www.ipc.org/system/files/technical_resource/E40%26S02_02%20-%20Jesse%20Greenwood%20.pdf.
44. Dubourg, G. et al. Flexible and highly sensitive humidity sensors using screen-printed TiO2 nanoparticles as sensitive layer. *J. Phys.: Conf. Ser.* **939**, 012008 (2017).
45. Kim, N. W., Lee, D.-G., Kim, K.-S. & Hur, S. Effects of Curing Temperature on Bending Durability of Inkjet-Printed Flexible Silver Electrode. *Nanomaterials* **10**, 2463 (2020).
46. Rao, B. G., Mukherjee, D. & Reddy, B. M. CHAPTER 1: NOVEL APPROACHES FOR PREPARATION OF NANOPARTICLES. In *Nanostructures in Therapeutic Medicine Series. Nanostructures for Novel Therapy Synthesis, Characterization and Applications*, **1**, 875 (Elsevier, Bucharest, Romania, 2017).
47. Koshi, T., Nomura, K.-i & Yoshida, M. Resistance Reduction of Conductive Patterns Printed on Textile by Curing Shrinkage of Passivation Layers. *Micromachines* **11**, 539 (2020).
48. Joshi, S. R. et al. Low-cost and fast-response resistive humidity sensor comprising biopolymer-derived carbon thin film and carbon microelectrodes. *J. Electrochem. Soc.* **167**, 147511 (2020).

49. Schubert, M. et al. Novel Method for NTC Thermistor Production by Aerosol Co-Deposition and Combined Sintering. *Sens. (Basel, Switz.)* **19**, 1632 (2019).
50. Arman Kuzubasoglu, B. Recent Studies on the Humidity Sensor: A Mini Review. *ACS Appl. Electron. Mater.* **4**, 4797–4807 (2022).
51. Phung, T. H. et al. IoT device fabrication using roll-to-roll printing process. *Sci. Rep.* **11**, 19982 (2021).
52. Duan, Z. et al. Facile, Flexible, Cost-Saving, and Environment-Friendly Paper-Based Humidity Sensor for Multifunctional Applications. *ACS Appl. Mater. Interfaces* **11**, 21840–21849 (2019).
53. Jang, J. H. & Han, J. I. Cylindrical relative humidity sensor based on poly-vinyl alcohol (PVA) for wearable computing devices with enhanced sensitivity. *Sens. Actuators A: Phys.* **261**, 268–273 (2017).
54. Li, Z. et al. The Effect of Surface Hydroxyls on the Humidity-Sensitive Properties of LiCl-Doped ZnSn(OH)6 Sphere-Based Sensors. *Nanomaterials* **12**, 467 (2022).
55. Yoo, K.-P. et al. Novel resistive-type humidity sensor based on multiwall carbon nanotube/polyimide composite films. *Sens. Actuators B: Chem.* **145**, 120–125 (2010).
56. Jiang, K., Fei, T., Jiang, F., Wang, G. & Zhang, T. A dew sensor based on modified carbon black and polyvinyl alcohol composites. *Sens. Actuators B: Chem.* **192**, 658–663 (2014).
57. Dai, H., Feng, N., Li, J., Zhang, J. & Li, W. Chemiresistive humidity sensor based on chitosan/zinc oxide/single-walled carbon nanotube composite film. *Sensors and Actuators B: Chemical* **283**, 786–792 (2018).
58. Jung, U. H., Park, K. T., Park, E. H. & Kim, S. H. Improvement of low-humidity performance of PEMFC by addition of hydrophilic SiO2 particles to catalyst layer. *J. Power Sources* **159**, 529–532 (2006).
59. Liu, H. et al. Relative Humidity Sensor Based on S-Taper Fiber Coated With SiO2 Nanoparticles. *IEEE Sens. J.* **15**, 3424–3428 (2015).
60. Xu, B. & Zhang, Q. Preparation and Properties of Hydrophobically Modified Nano-SiO2 with Hexadecyltrimethoxysilane. *ACS Omega* **6**, 9764–9770 (2021).
61. Duan, Z.-H. et al. Enhanced positive humidity sensitive behavior of p-reduced graphene oxide decorated with n-WS2 nanoparticles. *Rare Metals* **40**, 1762–1767 (2020).
62. Viegas, D. et al. A fibre optic humidity sensor based on a long-period fibre grating coated with a thin film of SiO2 nanospheres. *Meas. Sci. Technol.* **20**, 034002 (2009).
63. Gomez, D., Morgan, S. P., Hayes-Gill, B. R., Correia, R. G. & Korposh, S. Polymeric optical fibre sensor coated by SiO2 nanoparticles for humidity sensing in the skin microenvironment. *Sens. Actuators B: Chem.* **254**, 887–895 (2018).
64. Sachin, Pandey, B. K. & Jaiswal, R. L. Electrical conductivity of semiconducting nanoparticles. *Phys. B: Condens. Matter* **646**, 414279 (2022).
65. Park, S. et al. Capacitive humidity sensing properties of freestanding bendable porous SiO2/Si thin films. *Sci. Rep.* **12**, 11689 (2022).
66. Aldosky, H. Y. Y. & Shamdeen, S. M. H. A new system for measuring electrical conductivity of water as a function of admittance. *J. Electr. Bioimpedance* **2**, 86–92 (2010).
67. Vaussenat, F. et al. Continuous Critical Respiratory Parameter Measurements Using a Single Low-Cost Relative Humidity Sensor: Evaluation Study. *JMIR Biomed. Eng.* **8**, e47146 (2023). Company: JMIR Biomedical Engineering Distributor: JMIR Biomedical Engineering Institution: JMIR Biomedical Engineering Label: JMIR Biomedical Engineering Publisher: JMIR Publications Inc., Toronto, Canada.
68. Kano, S. et al. Respiratory Monitoring by Ultrafast Humidity Sensors with Nanomaterials: A Review. *Sensors* **22**, 1251 (2022).
69. Duan, Z., Jiang, Y. & Tai, H. Recent advances in humidity sensors for human body related humidity detection. *J. Mater. Chem. C.* **9**, 14963–14980 (2021).
70. Bhattacharjee, M., Nemade, H. B. & Bandyopadhyay, D. Nano-enabled paper humidity sensor for mobile based point-of-care lung function monitoring. *Biosens. Bioelectron.* **94**, 544–551 (2017).
71. Russo, M. A., Santarelli, D. M. & O'Rourke, D. The physiological effects of slow breathing in the healthy human. *Breathe* **13**, 298–309 (2017).
72. Arshad, B. et al. Computer Vision and IoT-Based Sensors in Flood Monitoring and Mapping: A Systematic Review. *Sens. (Basel, Switz.)* **19**, 5012 (2019).
73. Altenberend, U. et al. Towards fully printed capacitive gas sensors on flexible PET substrates based on Ag interdigitated transducers with increased stability. *Sens. Actuators B: Chem.* **187**, 280–287 (2013).
74. Qu, C., Hu, J., Liu, X., Li, Z. & Ding, Y. Morphology and Mechanical Properties of Polyimide Films: The Effects of UV Irradiation on Microscale Surface. *Materials* **10**, 1329 (2017).
75. Constantin, C. P., Aflori, M., Damian, R. F. & Rusu, R. D. Biocompatibility of Polyimides: A Mini-Review. *Mater. (Basel, Switz.)* **12**, 3166 (2019).
76. Santavirta, S. et al. Biocompatibility of silicon carbide in colony formation test in vitro. A promising new ceramic THR implant coating material. *Arch. Orthop. Trauma Surg.* **118**, 89–91 (1998).
77. Smith, A. D. et al. Resistive graphene humidity sensors with rapid and direct electrical readout. *Nanoscale* **7**, 19099–19109 (2015).
78. Tang, Q.-Y., Chan, Y. C. & Zhang, K. Fast response resistive humidity sensitivity of polyimide/multiwall carbon nanotube composite films. *Sens. Actuators B: Chem.* **152**, 99–106 (2011).
79. Zhang, D., Tong, J. & Xia, B. Humidity-sensing properties of chemically reduced graphene oxide/polymer nanocomposite film sensor based on layer-by-layer nano self-assembly. *Sens. Actuators B: Chem.* **197**, 66–72 (2014).
80. Su, C.-H. et al. Highly Responsive PEG/Gold Nanoparticle Thin-Film Humidity Sensor via Inkjet Printing Technology. *Langmuir: ACS J. Surf. colloids* **35**, 3256–3264 (2019).
81. Reddy, A. S. G. et al. Fully Printed Flexible Humidity Sensor. *Procedia Eng.* **25**, 120–123 (2011).
82. Zhang, X. et al. Printed Carbon Nanotubes-Based Flexible Resistive Humidity Sensor. *IEEE Sens. J.* **20**, 12592–12601 (2020).
83. Ali, S., Hassan, A., Hassan, G., Bae, J. & Lee, C. H. All-printed humidity sensor based on graphene/methyl-red composite with high sensitivity. *Carbon* **105**, 23–32 (2016).
84. Yan, F.-J. et al. Direct ink write printing of resistive-type humidity sensors. *Flex. Print. Electron.* **6**, 045007 (2021).
85. Connolly, E., Pham, H., Groeneweg, J., Sarro, P. & French, P. Silicon carbide membrane relative humidity sensor with aluminium electrodes. In *17th IEEE International Conference on Micro Electro Mechanical Systems. Maastricht MEMS 2004 Technical Digest*, 193–196 (2004).

Acknowledgements

The authors would like to thank Paul Fourmont for his mentorship towards the experimental plan. Mohammad Sadaati for performing the SEM and EDX analysis and Josianne Lefebvre for performing the XPS analysis. S.G.C. would like to thank the IRSST, the NSERC-Discovery program and the Canada Research Chair program for their financial support for this project.

Author contributions

A.W. conceived the ink fabrication methodology, experimental plan, performed all experiments and wrote the manuscript, A.P. designed and tested the KN95 mask and hand test applications, M.H.T assisted with the printing of all test patterns and devices, A.Z assisted with performing FTIR and XRD analysis, J.B.G performed Raman spectroscopy, high resolution optical imaging and reviewed the manuscript, M.G wrote all matlab codes for data processing, F.V conceptualized and supervised the KN95 mask application, M.B supervised the experimental plan and implementation

along with manuscript review, S.G.C supervised the entire project and provided the funding source. All authors reviewed the manuscript and given approval to the final version.

Competing interests
The authors declare no competing interests.

Consent for publication
All authors have given their consent.

Ethics approval and consent to participate
All authors have given their consent and do not have any conflict of interest. The authors verify due consent was obtained from the participant (second author) in the KN95 mask study and all the ethical regulations established by ETS were followed during the study.

Additional information
Supplementary information The online version contains supplementary material available at https://doi.org/10.1038/s44172-025-00425-2.

Correspondence and requests for materials should be addressed to Sylvain G. Cloutier.

Peer review information *Communications Engineering* thanks Fan Liu, Yuqing Meng, and the other, anonymous, reviewer for their contribution to the peer review of this work. Primary Handling Editors: [Jianhua (Joshua) Tong] and [Miranda Vinay and Rosamund Daw].